Adv. Opt. Mater.

Strong Coupling of Self-Trapped Excitons to Acoustic Phonons in Bismuth Perovskite $Cs_3Bi_2I_9$

*Xing He, Naveen K. Tailor, Soumitra Satapathi, Jakoah Brgoch, Ding-Shyue Yang**

X. He, J. Brgoch, D.-S. Yang
Department of Chemistry, University of Houston, Houston, Texas 77204, United State of America.

N. K. Tailor, S. Satapathi
Department of Physics, Indian Institute of Technology Roorkee, Roorkee, Uttarakhand 247667, India.

J. Brgoch
Texas Center for Superconductivity, University of Houston, Houston, Texas 77204, United State of America.

*To whom correspondence should be addressed. Email: yang@uh.edu

Abstract

To assess the potential optoelectronic applications of metal-halide perovskites, it is critical to have a detailed understanding of the nature and dynamics of interactions between carriers and the polar lattices. Here, we report the electronic and structural dynamics of bismuth-based perovskite $Cs_3Bi_2I_9$ revealed by transient reflectivity and ultrafast electron diffraction. A cross-examination of these results combined with theoretical analyses allows the identification of the major carrier–phonon coupling mechanism and the associated time scales. It is found that carriers photoinjected into $Cs_3Bi_2I_9$ form self-trapped excitons on an ultrafast time scale. However, they retain most of their energy and their coupling to Fröhlich-type optical phonons is limited at early times. Instead, the long-lived excitons exert an electronic stress via deformation potential and develop a prominent, sustaining strain field as coherent acoustic phonons in 10 ps. From sub-ps to ns and beyond, a similar extent of the atomic displacements is found throughout the different stages of structural distortions, from limited local modulations to a coherent strain field to the Debye–Waller random atomic motions on longer times. The current results suggest the potential use of bismuth-based perovskites for applications other than photovoltaics to take advantage of carriers' stronger self-trapping and long lifetime.

Keywords: electron–phonon coupling, lead-free halide perovskites, time-resolved carrier and structural dynamics

1. Introduction

Research activities on metal-halide perovskites (MHPs) have escalated exponentially over the past decade, with tremendous attention especially on their optoelectronic performances but also on other opportunities such as energy storage, radiation detection and photocatalysis.[1] Fundamentally, wide-ranging compositions, crystal structures, electronic properties, and carrier mobilities and lifetimes with different dimensionalities are seen among the great number of MHPs that have been synthesized.[1d, 1e] At the heart of their optoelectronic phenomena, dynamical behaviors including ultrafast carrier dynamics,[2] carrier–phonon couplings,[3] motions of organic cations,[4] and lattice dynamics[5] require many detailed studies for a coherent understanding. Time-resolved pump-probe techniques are particularly crucial to further reveal the interplays among the many essential factors. For example, a number of ultrafast studies took a closer look at the nature of the interactions between photoinjected carriers and the polar lattice of a MHP bulk to understand charge relaxation and transport. The formation of Fröhlich-type large polarons has been recognized as a leading mechanism for long-lived carriers in lead-halide perovskites (LHPs).[6] In single-crystalline $CH_3NH_3PbI_3$, Mante *et al.* discussed about the coupling between photoinjected charges and acoustic phonons, although the amplitude of the coherent acoustic phonon (CAP) signal is two orders-of-magnitude lower than that of the initial electronic response from transient reflectivity.[7] Very recently, visualization of the dynamic lattice distortions on the nanoscale, including excitation-induced polarons and later-time CAPs, was achieved by using ultrafast x-ray diffuse scattering and diffraction measurements on $CH_3NH_3PbBr_3$.[5] These studies and many others have offered illuminating insights about LHPs, which are frequently used in the comparisons with the properties and behavior of newly developed MHPs.

The toxicity and stability of lead-containing compounds and strong regulatory requirements for their use in consumer products have prompted the search for environmentally-friendly lead-free MHPs with comparable optoelectronic performances.[8] Bismuth-based MHPs received notable attention because they can address the aforementioned concerns. However, the strong interactions between carriers and the polar lattice of Bi-based semiconductors appear to fundamentally limit their optoelectronic performances.[9] Specifically, Wu *et al.* reported experimental evidence from time-resolved optical spectroscopy measurements to infer strong carrier self-trapping in $Cs_2AgBiBr_6$ via deformation potential coupling with acoustic phonons,

thus casting doubts on the potential photovoltaic use of Bi-based double perovskites with a soft lattice.[10] However, no diffraction-based direct probing of the structural dynamics has been reported for Bi-based MHPs to date.

Here, using transient reflectivity (TR) and ultrafast electron diffraction (UED), we present the experimental results for the electronic and structural responses of $Cs_3Bi_2I_9$, a quasi-zero-dimensional (quasi-0D) MHP with separated bioctahedral $[Bi_2I_9]^{3-}$ units, following the above-gap injection of photocarriers. A cross-examination of both the optical and diffraction data is critical to revealing the nature of carrier–lattice interactions on ultrashort time scales. The immediate exciton self-trapping in $Cs_3Bi_2I_9$ without much local structural distortion in the first 10 ps indicates a limited coupling to the optical phonons and the retaining of most energy by the trapped carriers without extensive, large-polaronic relaxation. However, the prominent CAPs observed by TR signify a strong coupling of carriers with the acoustic phonons via deformation potential in the first 10 ps, resulting in a strain field persistent beyond the experimental observation window. Additionally, the injected photocarriers at an 8% excitation level are surprisingly long-lived, whose annihilation and nonradiative energy transfer causes the increase of the lattice temperature and therefore random atomic motions on sub-ns to ns time.

2. Results

Optical absorption and photoluminescence spectra of $Cs_3Bi_2I_9$ crystals have been reported in the literature,[11] where the exciton binding energy E_b was found to be high at ~300 meV.[12] Built on such near-steady-state knowledge, the current report is focused on dynamic carrier–structure coupling on ultrashort timescales. Time-resolved information acquired by complimentary methods—TR and UED, which are directly sensitive to photocarriers and atomic displacements/motions, respectively—needs to be cross-examined to obtain a coherent physical picture for both the electronic and lattice dynamics. In what follows we first describe the results derived from each method and then discuss their correlations.

2.1. Transient reflectivity of $Cs_3Bi_2I_9$: Self-trapped excitons and coherent acoustic phonons

Shown in **Figure 1** are the TR results measured in ultrahigh vacuum from freshly cleaved (001) surfaces of crystalline $Cs_3Bi_2I_9$, where the injection of photocarriers is made by using 515-nm light. Given that the energy dispersion of the electronic bands of $Cs_3Bi_2I_9$ is small[13] and the photon energy of E_{ex} = 2.41 eV matches with the vertical transitions across the gap reasonably well, the above-gap photoexcitation results in an initial injection of carriers over a broad range in

the Brillouin zone (Figure S1). The wavelength of the probe beam is centered at λ_{pr} = 1030 nm, whose photon energy of 1.2 eV is appreciably lower than the indirect band gap. Hence, according to the developed theory for carriers in a semiconductor band picture,[14] the anticipated optical pump–probe TR observation would be prominent early-time changes with electronic origins followed by relaxation dynamics and (often smaller) lattice contributions resulting from carrier–phonon coupling. Such results have been seen and analyzed for conventional photovoltaic semiconductors such as silicon, gallium arsenide, and cadmium chalcogenides.[15] However, instead, the TR dynamics of $Cs_3Bi_2I_9$ show an initial change limited in both magnitude and duration followed by prominent and persistent periodic modulations over the measured temporal window (Figure 1a). These TR features indicate that $Cs_3Bi_2I_9$ behaves significantly differently from typical semiconductors following photoexcitation. The question is, how different are the photodynamics of $Cs_3Bi_2I_9$?

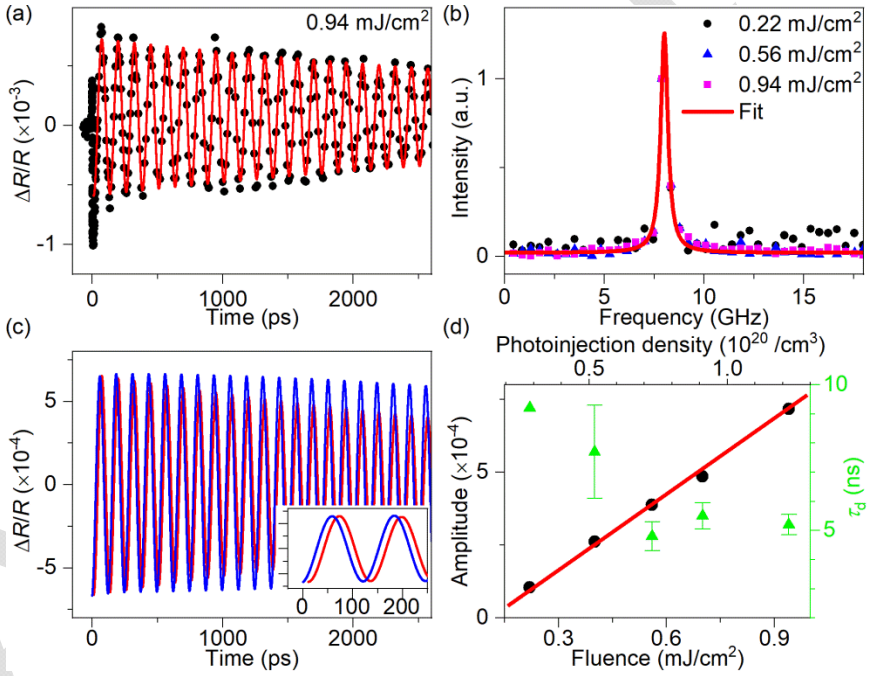

Figure 1. Transient reflectivity measured from $Cs_3Bi_2I_9$(001). (a) Prominent, persisting periodic modulations due to carrier-induced CAPs. The red curve is a fit using Equation 1. (b) Fourier-transformed spectrum (normalized to the peak data point) of the oscillatory signals acquired at three different fluences. The red curve is a Lorentzian fit centered at the frequency matching the period in (a). (c) Comparison of the experimental (red) and theoretical (blue) CAP results. The inset shows the early-time range. The ~10-ps shift between the two curves signifies the CAP coupling and development time. (d) Fluence dependence of the amplitude (black dots) and decay time (green triangles) of the CAP periodic modulations. The red line is a linear fit intercepting at the origin.

We first examine the oscillatory signal, whose period is more than two orders of magnitude longer than those of relevant optical phonon modes[11a] and hence is not related to impulsive stimulated Raman scattering.[10] At the excitation fluence of 0.94 mJ cm^{-2}, the clear oscillation in the TR trace ($\Delta R/R \sim 10^{-3}$) is due to the interference between the reflected probe beams from the crystal surface and a strain pulse propagating into the bulk at the longitudinal speed of sound $v_{s,\parallel}$.[16] Such laser-induced strain pulses are termed coherent acoustic phonons (CAPs), which arise from the electronic and thermal stresses owing to, respectively, the deformation potential coupling due to long-lived photocarriers and the thermoelastic effect by the excess energy following carrier–phonon coupling and carrier relaxation.[16] A fit of the periodic modulations to the model

$$\frac{\Delta R(t)}{R_0} = A_{\mathrm{osc}} \cos\left(\frac{2\pi t}{\tau_{\mathrm{osc}}} - \phi\right) \exp\left(-\frac{t}{\tau_d}\right) \quad (1)$$

yields the initial amplitude A_{osc} = (7.17±0.12)×10^{-4}, the period τ_{osc} = 124.9±0.1 ps, the phase ϕ = 0.52 (equivalent to an onset time of oscillation $t_{0,\mathrm{osc}} \approx$ 10 ps), and the dephasing time $\tau_{\mathrm{d}} \approx$ 5 ns that exceeds the observed temporal window (Figure 1a). The Fourier-transformed spectrum also shows a single peak at $1/\tau_{\mathrm{osc}}$ = 8.006 GHz, which is independent of the fluence used at room temperature (Figure 1b). Hence, based on the experimental condition,

$$\tau_{\mathrm{osc}} = \frac{\lambda_{\mathrm{pr}}}{2 v_{s,\parallel} \sqrt{n_0^2 - \sin^2 \theta_{\mathrm{in}}}} \quad (2)$$

where the incidence angle of the probe beam is θ_{in} = 35° and the refractive index n_0 at λ_{pr} = 1030 nm is assumed to be in the range of 2.08[13a] to 2.20,[17] and we obtain $v_{s,\parallel}$ = 1.94 to 2.06 km s^{-1} in good agreement with previous reports[17-18] and comparable to (or slightly lower than) that of $CH_3NH_3PbI_3$[7] and bismuth-based double perovskite $Cs_2AgBiBr_6$.[10] Additionally, we find that A_{osc} is linearly dependent on the initial photoinjection density, whereas the dephasing time is similar in the fluence range used or slightly increased at a lower photoexcitation level (Figure 1d).

We conduct theoretical calculations to further understand the origin and magnitude of the prominent CAPs. Given the material's band gap of $E_g \cong$ 1.9 eV,[19] the ratio between the electronic and thermal stresses is approximately given by $(\partial E_g/\partial p)\rho C/[3\beta(E_{\mathrm{ex}} - E_g)]$ with the mass density ρ = 5.02 g cm^{-3}, the specific heat $C \approx$ 0.178 J g^{-1} K^{-1} as in the high-temperature limit, and the thermal expansion coefficient β = 4.8×10^{-5} K^{-1}.[11a, 18, 20] However, as will be

shown later from the UED results, carriers still retain most of the above-gap excess energy and effectively diminish $E_{\mathrm{ex}} - E_g$ in the denominator. This signifies the dominance of the electronic stress if the carriers have a sufficiently long lifetime.[16] Shown in Figure 1c is the comparison of the experimentally observed periodic modulations with the theoretical curve (see Table S1 for the parameters used), which assumes an instantaneous and persisting lattice deformation and involves a finite spectral width of the probe beam.[16b] Two points are worth noting. First, the offset in ϕ (and hence non-instantaneous, nonzero $t_{0,\mathrm{osc}}$; see also **Figure 2**, a and c) signifies the time of ~10 ps needed for the carriers' coupling to CAPs to mature, which is significantly longer than the typical carrier relaxation time toward band edges as well as the offset time observed in conventional semiconductors.[16b] Such a result hints the limitation of the use of a band picture for the photodynamics of $Cs_3Bi_2I_9$ (see below). Second, the observed dephasing cannot be accounted for by the limited attenuation resulting from the finite probe bandwidth.[16b] Beside the possible minor inhomogeneity inside the crystalline sample, the loss of carriers (and hence the reduction in the electronic stress and its conversion into thermoelastic stress that has a different CAP amplitude factor and may not be fully in-phase), thermal diffusion (which alters the thermoacoustic pulse shape over time[16a]), and residual below-gap absorption due to the existence of defects (and therefore an attenuation of the probe beam) may also cause the decrease of the reflected signal. We estimate an upper bound of ~500 cm^{-1} at 1030 nm by translating τ_{d} into a round-trip effective depth. Given that τ_{d} is about an order of magnitude larger than the carrier lifetime (i.e., the annihilation of carriers and their energy transfer to the lattice; see below), the longer dephasing time observed at a low fluence (Figure 1d, green) might signify, at a lower temperature jump and therefore gradient, less nonlinear dephasing over time due to sample inhomogeneity, the electronic–thermoelastic stress conversion, and/or thermal diffusion.

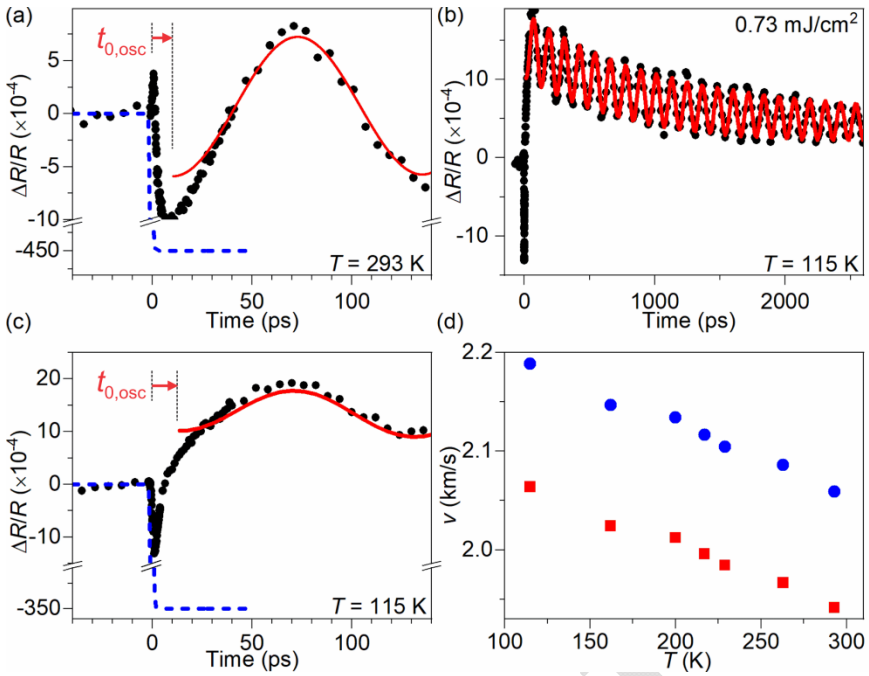

Figure 2. Transient reflectivity at early times and select temperatures. (a) Comparison between the experimental results (black dots) and the theoretical free-carrier absorption (blue dashed line) at room temperature. The red curve is the same as that in Figure 1a with the onset time of oscillation $t_{0,\mathrm{osc}}$ indicated. (b) Transient reflectivity measured at 115 K. The red curve is a fit using Equation 1. (c) Early-time dynamics of (b), with a similar $t_{0,\mathrm{osc}}$ and the theoretical free-carrier absorption shown as the blue dashed line. (d) Temperature dependence of the longitudinal speed of sound obtained from the oscillation period using Equation 2. The blue and red points at a temperature indicate the range calculated using different values for the refractive index.

We now turn our attention to the initial TR signal, which provides further insights into the nature and dynamics of the injected photocarriers. With the *s*-polarized probe,

$$\frac{\Delta R}{R_0} = \mathrm{Re}\left(\frac{4n_0 \cos\theta_{\mathrm{in}}}{(n_0^2-1)\sqrt{n_0^2-\sin^2\theta_{\mathrm{in}}}} \cdot \Delta n\right). \tag{3}$$

For conventional semiconductors with a band picture, three carrier-induced changes to the index of refraction (Δn) can be modeled for a below-gap probe wavelength: free-carrier absorption (i.e., plasma effect) and band-filling (Bursteirn–Moss effect) give negative contributions, whereas bandgap renormalization leads to a positive change.[14] This means that a negative TR signal is anticipated due to free-carrier absorption within hundreds of fs to first ps before photocarriers reach thermalization near the band edges and the contributions from the other two effects become fully matured. At a 515-nm fluence of 0.94 mJ cm^{-2}, we estimate an average photoinjection density of $N_0 \cong 1.2\times10^{20}$ cm^{-3} electron–hole pairs within the optical probed range

$\lambda_{pr}/4\pi|n_0| \cong 40$ nm and hence anticipate a large initial reflectivity drop $\Delta R/R_0 \cong -4.5\%$ from $Cs_3Bi_2I_9$ (see Supplementary Information for the equations and calculations). However, the opposite sign with a magnitude two orders lower is observed at room temperature (Figure 2a); similar observations at a much lower laser fluence were reported.[19b] In fact, the initial peak and the oscillatory amplitude A_{osc} are nearly comparable as opposed to those of $Cs_2AgBiBr_6$ and $CH_3NH_3PbBr_3$ with a clearly lower oscillation-to-peak ratio (see Figure S13 of Ref. [10]). At a low temperature T = 115 K, the sign of the initial TR change appears to be consistent with the free-carrier absorption contribution, but the magnitude is still ~1.5 orders lower than theoretically predicted (Figure 2, b and c; see Supplementary Information and Figure S2 for an additional discussion about the temperature-related differences in the TR).

Such TR observations signify that photoinjected electrons and holes lose their initial free-carrier nature on an ultrashort time scale. This is consistent with the proposed picture of trapping of excitons by the lattice (small polarons) based on steady-state results;[11a] here, we find the appearance of bound excitons in $Cs_3Bi_2I_9$ to be nearly immediate such that the self-trapped condition effectively removes carriers from the plasma and therefore results in the notable failure of the free-carrier model under a band picture at initial times. The finding is also in line with those for bismuth double perovskite $Cs_2AgBiBr_6$,[10] but we consider stronger trapping in $Cs_3Bi_2I_9$ given the more significantly diminished initial electronic response versus the amplitude of the CAP signal. If we follow the generally accepted picture that thermalization of the photocarriers is typically reached on the sub- to few-ps time, such a quasi-equilibrium (though across the bandgap) allows the use of the Saha equation from an energetic viewpoint to estimate the ratio between the photoexcited bound excitons (n_{EX} as the density) and unbound electron-hole plasma ($n_{e,h}$ as the density),

$$\frac{n_{e,h}^2}{n_{EX}} = \left(\frac{2\pi\mu_{EX}k_BT}{h^2}\right)^{3/2} e^{-E_b/k_BT} \quad (4)$$

where μ_{EX} is the effective reduced mass, k_B the Boltzmann constant, and h the Planck constant.[21] For the ranges of photoinjection density and sample temperature used here, $n_{e,h}$ is many orders of magnitude smaller than n_{EX} given that E_b is close to 300 meV.[12] Thus, the experimental results again support the theoretical model that essentially all photoinjected carriers quickly form bound excitons, which may have its origin in the quantum confinement effect from the quasi-0D bioctahedral $[Bi_2I_9]^{3-}$ units.[12a] The structural phase transition at 220 K[22] does not

appear to cause major effects on the photodynamics. The longitudinal speed of sound derived from τ_{osc} at different temperature is shown in Figure 2d, whose dependence agrees well with a previous report for a polar lattice.[18]

With the knowledge of ultrafast carrier trapping and CAPs, the following is to examine the details of carrier–phonon coupling and the corresponding dynamics. In conventional inorganic semiconductors, the initial coupling is often via optical phonons followed by phonon scattering and thermalization in the acoustic branches. In MHPs, the Fröhlich interaction between carriers and longitudinal optical (LO) phonons has been considered crucial.[6c, 23] We obtain the coupling constants of ~3.0 for electrons and ~3.4 for holes, averaged from the calculated values using different effective masses and dielectric constants reported in the literature (see Table S1 for the parameters used) with the A_1' symmetric stretch of terminal Bi–I bonds.[11a] The results correspond to the large-intermediate Fröhlich coupling similar to those for $CsPbBr_3$[6c] and $Cs_2AgBiBr_6$.[10] Thus, from the viewpoint of LO-phonon coupling, it may not be clear why $Cs_3Bi_2I_9$ exhibits distinct dynamics with prominent CAPs and very limited initial electronic TR response. The onset time difference of ~10 ps between the photoinjection and the CAP signal (Figure 2, a and c) may presumably be viewed as the duration for the initial carrier–LO phonon coupling. However, the UED results presented below reveal that LO phonons may not play a dominant role.

2.2. **Ultrafast electron diffraction of $Cs_3Bi_2I_9$(001)**

We use UED in reflection geometry to directly probe and reveal the phonon dynamics of $Cs_3Bi_2I_9$ at 115 K. Shown in **Figure 3**a is a diffraction image with the use of a gently converging beam (to achieve the smallest probe footprint on the sample) without photoexcitation. Multiple orders of (006) are seen along the center streak and both (10) and (11) in-plane zones are visible (the in-plane indices follow the room-temperature structure for simplicity). This pattern shows that the freshly cleaved surface is (001) with ordered stacking along the surface normal *c* axis, whereas the crystal growth along the horizontal directions involves multiple zones and hence crystalline domains of the low-temperature phase. In addition, the transmission-like pattern signifies probing electrons passing through and being diffracted from nm-scaled roughness.[24] Therefore, we concentrate on the changes of the $(00l)$ intensities as a function of delay time, which are directly affected by the out-of-plane components of laser-initiated atomic motions.

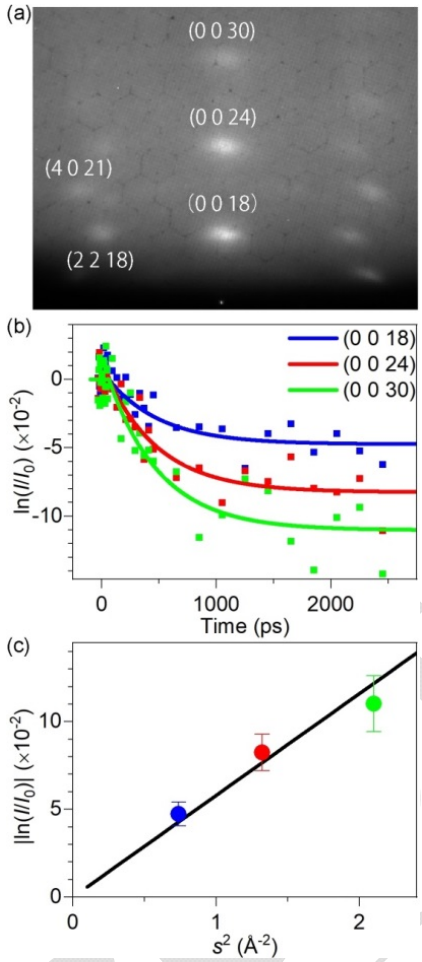

Figure 3. UED results measured from $Cs_3Bi_2I_9$(001) at 0.94 mJ/cm^2. (a) Diffraction image recorded at 115 K without photoexcitation. Miller indices are assigned for select Bragg spots. (b) Time-dependent intensity changes of the center three diffraction spots. The solid curves are fits of a single-exponential decay function. (c) Dependence of the intensity decrease on $s_{\parallel}^2$. The black line is a linear fit intercepting with the origin. The error ranges are ±2 standard deviations obtained from the fits in (b).

Surprisingly, we do not observe the anticipated fast intensity changes in the first few tens of ps that are very common in UED studies of perovskites[25] and other materials.[26] Instead, the diffraction intensities decrease over a much longer time, whose fits to a single-exponential function yield the long time constant of ~450 ps (Figure 3b). After ~2 ns, the intensity drops reach the full extent and remain so within the observed temporal window. We confirm the structural origin, not any surface transient electric field effect, for the observed diffraction changes. This is evidenced in Figure 3c by the linear relation between $\ln[I_0/I(t)]$ and $s_{\parallel}^2$, where I_0 and $I(t)$ are, respectively, the intensities of a diffraction spot before the zero of time and at

time t after excitation and $s_{\parallel} = l \cdot c^*$ is the momentum transfer parallel to the surface normal ($c^* = 1/c$ = 0.0472 Å^{-1} is the corresponding reciprocal primitive cell length; see Supplementary Information for further discussion about Debye–Waller-type random atomic motions).[26b, 26d, 27] Additionally, we do not notice clear differences in the time-dependent changes of side Bragg spots such as (2 2 18) and (4 0 21).

The aforementioned time-dependent diffraction changes reveal multiple unique features of the photoinduced structural dynamics of $Cs_3Bi_2I_9$. First, according to the general understanding of carrier–phonon coupling, if the band picture is adequate for a photoexcited material, at least the excess energy above the bandgap ($E_{\mathrm{ex}} - E_g$ per photon) should be quickly transferred to the lattice, which would result in thermal atomic motions and hence cause diffraction intensities to decrease at a rate characteristic of a material's phonon–phonon scattering and thermalization time. If materials also exhibit a short carrier lifetime through nonradiative recombination, the bandgap energy per carrier pair is further released to the lattice, which leads to more atomic motions.[27] The lack of notable intensity changes for $Cs_3Bi_2I_9$ in the first few tens of ps, however, signifies both the breakdown of the band picture and a long carrier lifetime. Thus, the increase in the atomic motions, especially the randomized thermal motions, is limited in the first few tens of ps. This finding is in fact fully consistent with what the early-time TR results have revealed about the ultrafast formation of self-trapped excitons and no free carriers, which strengthens the view of $Cs_3Bi_2I_9$ as a "molecular" crystal not only from the structural but also behavioral standpoints. In this regard, a structural modulation of the ionic lattice for the trapped carriers may retain appreciable excess energy, as depicted by the displaced harmonic oscillator diagram with a large Huang–Rhys factor.[11a] Moreover, the long-lasting excitons cause an electronic stress that leads to the formation of CAPs observed in TR.

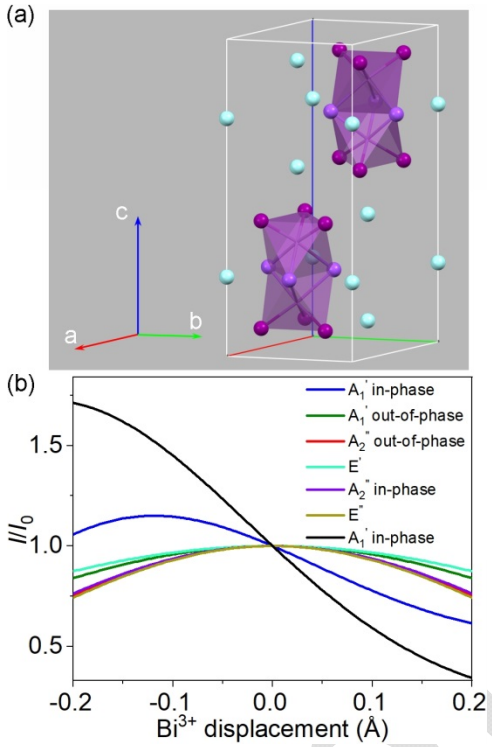

Figure 4. Structure of $Cs_3Bi_2I_9$ and diffraction simulations. (a) Unit cell showing the two $[Bi_2I_9]^{3-}$ units with Cs in light blue, terminal I in dark purple, and bridge I in light purple. The bismuth atoms (not shown) are at the centers of the octahedral frameworks. (b) Simulated changes of the (0 0 24) diffraction intensity as a result of lattice distortions following select optical phonons. An atomic displacements of more than a few pm should lead to a noticeable intensity decrease in UED.

Second, we further note that the occupation number of LO phonons for the initial coupling and trapping of carriers should be limited in the first 10 ps. Here the intracell LO phonons (i.e. at Γ) are considered in accordance with the proposed small-polaron picture.[11a] Shown in **Figure 4**b are the simulated diffraction changes as a result of select major intracell optical phonon modes that have atomic displacements along the *c* axis, with A_1' terminal Bi–I symmetric stretch (in-phase and out-of-phase between the two $[Bi_2I_9]^{3-}$ units), A_2'' terminal Bi–I symmetric stretch (in-phase and out-of-phase), E' and E'' terminal Bi–I asymmetric stretch, and in-phase A_1' bridge Bi–I symmetric stretch.[11a, 28] A 5% range of the Bi–Bi distance of 4.042 Å is considered for the movement of a single Bi atom, which is ~3/4 of the root-mean-square displacement $\sqrt{B/8\pi^2}$ deduced from the equilibrium thermal factor B at low temperature.[29] Hence, to have a negligible effect on the $(00l)$ intensities, the increase in the optical phonon populations and consequently the atomic displacements needs to be small. (The coupling to the

modes of in-phase A_1' terminal and bridge Bi–I symmetric stretch may be larger given that a more linear dependence around the zero displacement is seen for the blue and black lines in Figure 4b. However, phonon–phonon scattering on a ps time scale should lead to the population of other phonon modes that can cause the diffraction intensities to decrease.) This appears to in contrast with the extent of the average optical-phonon atomic displacement suggested by the large Huang–Rhys factor of $S = 79.5$ should the lattice fully relaxes:[11a] considering the in-phase A_1' terminal Bi–I symmetric stretch at 146.6 cm^{-1} (ω_{LO} is the corresponding angular frequency), the carrier–phonon coupling-induced shift Δ can be estimated by $S = \omega_{LO}\Delta^2/2\hbar$, which gives a sub-Å value that is apparently too large according to the UED results. Thus, this finding provides the structural evidence for a shared and less dominant role played by the LO phonons' initial coupling to the photoinjected carriers. A similar view was also suggested for bismuth double perovskite $Cs_2AgBiBr_6$, although derived from optical spectroscopic data only.[10]

Third, the diffraction intensity decrease $\ln[I(t)/I_0]$ at longer times and its linear dependence on $s_{\parallel}^2$ indicate the increased thermal motions on the sub-ns to ns time. The thermal energy must come from the carriers. Thus, the time constant of ~450 ps in Figure 3b is attributed to the nonradiative recombination time of the trapped excitons at the photoinjection level of ~10^{20} cm^{-3}; it is also noted that an exponential-decay component exists on the sub-ns to ns time in low-temperature TR (Figure 2b). A similar lifetime has been reported although at a much lower carrier density.[30] Neglecting carrier diffusion and assuming that most photocarriers undergo the nonradiative process to release their energy to the lattice, we estimate from Figure 3c ~0.038 Å as the increase in the root-mean-square out-of-plane atomic displacement at the sample surface. This value is comparable to the initial electronic lattice strain of 2.3×10^{-3} at the surface deduced from the CAP modulations in the TR data, which is ~0.05 Å along *c* per unit cell (see Supplementary Information).

3. Discussion

Thus, a picture emerges for the photodynamics of $Cs_3Bi_2I_9$ after both the TR and UED results are taken into account. In the initial stage, the fact that the injected photocarriers are essentially localized coincides well with the quasi-0D nature of unconnected $[Bi_2I_9]^{3-}$ units and the electronic wavefunctions involved in the photoexcitation, from mainly iodide *p* orbitals to bismuth/iodide *p* molecular orbital states.[13] Such an electronic excitation (at a density of ~8% near the sample surface) is accompanied by local structural deformation (or, from the condensed-

matter standpoint, population of high-frequency optical phonons) centered on the excited $[Bi_2I_9]^{3-}$ units in the first several ps. Given such carrier–structure coupling, the excitonic atomic nudges should be directional and not random. However, their extent should be limited, up to a few pm per atom no more than ~1% of the Bi–I bond length, based on the UED result at early times. Transitioning in the next stage, an electronic stress via the deformation potential coupling is developed during the period up to ~10 ps, whose duration can be understood as the time needed to evolve from the more molecular-type excitons to lattice distortions coordinating all ions across a few unit cells, hence of the acoustic-phonon type. We note that a similar picosecond time scale was reported for the development of nanoscale polaronic distortions in $CH_3NH_3PbBr_3$, understood in a band picture together with the band-filling and bandgap renormalization effects.[5] In the current study of $Cs_3Bi_2I_9$, our data support the view of trapped carriers as local excitations (not separated electron and hole polarons) and the inadequacy of the band picture, in consistence with the quasi-0D nature.

The electronic stress caused by the long-lived excitons develops a strain impulse, which is launched in the surface region (highest near the surface because of the exponentially-decreasing depth profile of the carrier density) and propagates into the bulk at the longitudinal speed of sound. This CAP lattice distortion at the surface is about 5 pm per unit cell (see Supplementary Information for the estimate), which turns out to be of a similar extent as the earlier molecular deformation. In the final stage, the lattice temperature is elevated with more randomized atomic motions, as more and more carriers annihilate and transfer their energy to the lattice via nonradiative recombination at longer times on the sub-ns to ns scale. Incidentally, the Debye–Waller model yields a final motion increase of almost the same magnitude as the strain distortion (derived from Figure 3c; see Supplementary Information). Considering the origins for the structural motions in the three stages, our results indicate the evolution and organization of atomic motions from the more directional, coherent lattice displacements to longer-time incoherent, randomized thermal atomic motions, all of which show comparable magnitudes and have correlations with the injected carriers.

The ultrafast carrier–structure coupling resolved in this study may have implications for stimulated emission of MHPs with a similar dimensionality. In three-dimensional LHPs, the mechanism of lasing has been attributed to collective oscillations of an electron–hole plasma with negligible polaronic effects;[31] at lower carrier densities where large polarons are formed, it

is still reasonably valid to apply a band picture with the band-filling and bandgap renormalization effects being taken into account.[5] We note that the localized carrier and lattice dynamics of $Cs_3Bi_2I_9$ are very different from such a picture. A recent work demonstrated lasing phenomena (at *below-gap* wavelengths) by using microcrystals of a quasi-0D LHP Cs_4PbBr_6 illuminated with above-gap wavelengths, at fluences similar to the level used in this study.[32] The associated below-gap green photoluminescence (signifying the possibility of a population inversion) with a high quantum yield has been the subject of extensive studies.[33] We speculate that the lack of such lower-energy emission centers and the low photoluminescence quantum yield (as a result of molecular-type $[Bi_2I_9]^{3-}$ excitons and high nonradiative recombination) would be the fundamental bottlenecks for the use of $Cs_3Bi_2I_9$ as a lasing or photovoltaic material. Knowing that quantum dots of the bromide counterpart show more than two orders-of-magnitude higher photoluminescence quantum yield than the iodide compound,[34] it may be important to study the carrier–lattice coupling and structural dynamics of $Cs_3Bi_2Br_9$, which could exhibit crucial behavioral differences as a result of the nature of bonding in the $[Bi_2Br_9]^{3-}$ unit.

4. Conclusion

In summary, our results cross-examining time-resolved optical and direct structural measurements provide a detailed look at the coupling of photoinjected carriers to the crystal structure in bismuth-based halide perovskites. Strong carrier–structure coupling is found in $Cs_3Bi_2I_9$ following photoexcitation. Compared to lead-halide perovskites with a connected network, the photodynamics of $Cs_3Bi_2I_9$ is more of a molecular type due to the quasi-0D nature of the isolated $[Bi_2I_9]^{3-}$ units, which causes the electronic band picture to become inadequate. We find a limited coupling to the optical phonons and structural deformation in the first several ps. However, in the same duration of ~10 ps, the carrier-induced electronic stress via the deformation potential coupling is developed, leading to the launch of a propagating strain field as prominent coherent acoustic phonons. The sub-ns to ns decay of photocarriers eventually releases most of their energy and heats up the lattice to increase random atomic thermal motions. While the stronger self-trapping of carriers in bismuth-based MHPs compared to LHPs may pose a crucial limitation on their potential photovoltaic applications, this dynamic behavior with a long carrier lifetime may make them suitable for other uses such as radiation detection.[35]

5. Experimental Section

Sample Preparation: Single crystals of $Cs_3Bi_2I_9$ were grown using the inverse temperature crystallization technique described in Ref. [19b]. Their characterizations by scanning electron microscopy, energy dispersive x-ray spectroscopy, and x-ray photoelectron spectroscopy have been reported.[19b] To ensure the best surface quality for both TR and reflection UED measurements, mm-thick crystals were cleaved to produce a smooth (001) surface, which was quickly rinsed by chlorobenzene prior to the loading of the samples into the vacuum chamber assembly. All measurements were conducted in ultrahigh vacuum with a base pressure of the order of 10^{-10} torr to prevent the degradation of the cleaved sample surfaces.

TR and Reflection UED Measurements: Details about the TR and reflection UED apparatus has been previously described.[26b, 26d, 36] Briefly, the Yb:KGW regeneratively amplified laser system delivers a fundamental output of 170-fs pulses at 1030 nm. The 515-nm (2.41 eV) photoexcitation pulses produced by second harmonic generation (SHG) of the fundamental output were used in both the TR and UED measurements. A low photoinjection repetition rate of no more than 250 Hz with a fluence below 1 mJ/cm^2 was used in order to avoid optical surface damages, which was confirmed by no loss of optical reflectivity and electron diffraction intensities over many rounds of experiments. (Loss of intensities was noticed when the repetition rate was 500 Hz or higher or when a higher fluence was used at 250 Hz.) For TR, the fundamental output was used as the optical probe beam, whereas the excitation beam was mechanically chopped at half of the probe beam repetition rate. The surface-reflected probe beam was detected by a silicon photodiode connected to a lock-in amplifier for a phase-sensitive detection. For UED, another stage of SHG using a fraction of the 515-nm beam produced the ultraviolet (257 nm) pulses, which were focused on a LaB_6 emitter tip to generate photoelectron pulses accelerated to 30 keV. The electron diffraction images of the samples were produced at a grazing incidence angle and captured by an intensified CMOS camera assembly. A beam-front tilt setup was used to optimize the overall system response time for UED. However, the temporal resolution for TR measurements was affected and elongated to several hundred fs, which is not suitable for the detection of impulsive Raman signals that arise from the coupling to an optical phonon mode.

Density Functional Theory Calculations: Full structure optimizations and total energy calculations employed the Vienna *ab initio* simulation package (VASP) within the DFT framework.[37] The plane-wave basis set and projector augmented-wave (PAW) potentials were

used to define the electronic wave functions.[38] The crystal structure was first optimized using the Perdew-Burke-Ernzerhof (PBE) exchange and correlation functional[39] with the electronic convergence criteria set to 1×10^{-8} eV while the ionic relaxation was set to 1×10^{-2} eV Å^{-1}. A cutoff energy of 500 eV was used and the integration of the first Brillouin zone was carried out using a Monkhorst-Pack *k*-point grid of 9×9×3. Exchange and correlation was additionally described using the screened hybrid functional, HSE06.[40] The HSE06 functional was then implemented to correct for the significant underestimation of the PBE band gap with a Monkhorst-Pack *k*-point grid set to 4×4×2 and the electronic convergence criteria set to 1×10^{-8} eV. Phonon dispersion curves were calculated using the PHONOPY package, which uses the modified Parlinski-Li-Kawazoe *ab initio* force constant method.[41] Spin-orbit coupling was included in all calculations.

Supporting Information

Supporting Information is available from the Wiley Online Library or from the author.

Acknowledgements

This research was primarily supported by the R. A. Welch Foundation (E-1860). X.H. and the instrumental implementation of the pulse-front tilt scheme were partly supported by a National Science Foundation CAREER Award (CHE-1653903).

Author Contributions

D.-S.Y. conceived and supervised the project and wrote the manuscript; X.H. carried out the measurements and analyzed the results; N.K.T. and S.S. provided the single-crystalline samples; J.B. conducted the electronic band structure and phonon mode calculations. All authors were involved in the discussion of the results and contributed to the manuscript.

Conflict of Interest

The authors declare no competing financial interest. The University of Houston System requires the following statement: D.-S.Y. is a co-patent holder on US Patent No. 8,841,613.

Data Availability Statement

The data that support the findings of this study are available from the corresponding author upon reasonable request.

References

[1] a) M. A. Green, A. Ho-Baillie, H. J. Snaith, *Nat. Photonics* **2014**, *8*, 506-514; b) B. Saparov, D. B. Mitzi, *Chem. Rev.* **2016**, *116*, 4558-4596; c) J. P. Correa-Baena, M. Saliba, T. Buonassisi, M. Grätzel, A. Abate, W. Tress, A. Hagfeldt, *Science* **2017**, *358*, 739-744; d) R. L. Z. Hoye, J. Hidalgo, R. A. Jagt, J.-P. Correa-Baena, T. Fix, J. L. MacManus-Driscoll, *Adv. Energy Mater.* **2022**, *12*, 2100499; e) P. P. Jiang, D. Acharya, G. Volonakis, M. Zacharias, M. Kepenekian, L. Pedesseau, C. Katan, J. Even, *APL Mater.* **2022**, *10*, 060902.

[2] C. B. Li, A. L. Wang, X. Y. Deng, S. R. Wang, Y. Yuan, L. M. Ding, F. Hao, *ACS Photonics* **2020**, *7*, 1893-1907.

[3] Y. Yamada, Y. Kanemitsu, *NPG Asia Mater.* **2022**, *14*, 48.

[4] S. Y. Liu, R. Q. Guo, F. X. Xie, *Mater. Design* **2022**, *221*, 110951.

[5] B. Guzelturk, T. Winkler, T. W. J. Van de Goor, M. D. Smith, S. A. Bourelle, S. Feldmann, M. Trigo, S. W. Teitelbaum, H.-G. Steinrück, G. A. de la Pena, R. Alonso-Mori, D. L. Zhu, T. Sato, H. I. Karunadasa, M. F. Toney, F. Deschler, A. M. Lindenberg, *Nat. Mater.* **2021**, *20*, 618-623.

[6] a) X.-Y. Zhu, V. Podzorov, *J. Phys. Chem. Lett.* **2015**, *6*, 4758-4761; b) H. M. Zhu, K. Miyata, Y. P. Fu, J. Wang, P. P. Joshi, D. Niesner, K. W. Williams, S. Jin, X.-Y. Zhu, *Science* **2016**, *353*, 1409-1413; c) K. Miyata, D. Meggiolaro, M. T. Trinh, P. P. Joshi, E. Mosconi, S. C. Jones, F. De Angelis, X.-Y. Zhu, *Sci. Adv.* **2017**, *3*, e1701217.

[7] P. A. Mante, C. C. Stoumpos, M. G. Kanatzidis, A. Yartsev, *Nat. Commun.* **2017**, *8*, 14398.

[8] a) Z. J. Shi, J. Guo, Y. H. Chen, Q. Li, Y. F. Pan, H. J. Zhang, Y. D. Xia, W. Huang, *Adv. Mater.* **2017**, *29*, 1605005; b) F. Igbari, Z. K. Wang, L.-S. Liao, *Adv. Energy Mater.* **2019**, *9*, 1803150.

[9] S. R. Rondiya, R. A. Jagt, J. L. MacManus-Driscoll, A. Walsh, R. L. Z. Hoye, *Appl. Phys. Lett.* **2021**, *119*, 220501.

[10] B. Wu, W. H. Ning, Q. Xu, M. Manjappa, M. J. Feng, S. Y. Ye, J. H. Fu, S. Lie, T. T. Yin, F. Wang, T. W. Goh, P. C. Harikesh, Y. K. E. Tay, Z. X. Shen, F. Q. Huang, R. J. Singh, G. F. Zhou, F. Gao, T. C. Sum, *Sci. Adv.* **2021**, *7*, eabd3160.

[11] a) K. M. McCall, C. C. Stoumpos, S. S. Kostina, M. G. Kanatzidis, B. W. Wessels, *Chem. Mater.* **2017**, *29*, 4129-4145; b) Y. X. Zhang, Y. C. Liu, Z. Xu, H. C. Ye, Z. Yang, J. X. You, M. Liu, Y. H. He, M. G. Kanatzidis, S. Z. Liu, *Nat. Commun.* **2020**, *11*, 2304; c) N. K. Tailor, K. S. Saini, M. Kumar, S. Satapathi, *J. Phys. Chem. C* **2022**, *126*, 11165-11173.

[12] a) S. Rieger, B. J. Bohn, M. Döblinger, A. F. Richter, Y. Tong, K. Wang, P. Müller-Buschbaum, L. Polavarapu, L. Leppert, J. K. Stolarczyk, J. Feldmann, *Phys. Rev. B* **2019**, *100*, 201404; b) V. F. Machulin, F. V. Motsnyi, O. M. Smolanka, G. S. Svechnikov, E. Y. Peresh, *Low Temp. Phys.* **2004**, *30*, 964-967.

[13] a) M. Pazoki, M. B. Johansson, H. M. Zhu, P. Broqvist, T. Edvinsson, G. Boschloo, E. M. J. Johansson, *J. Phys. Chem. C* **2016**, *120*, 29039-29046; b) K.-H. Hong, J. Kim, L. Debbichi, H. Kim, S. H. Im, *J. Phys. Chem. C* **2017**, *121*, 969-974.

[14] B. R. Bennett, R. A. Soref, J. A. Del Alamo, *IEEE J. Quantum Electon.* **1990**, *26*, 113-122.

[15] a) A. J. Sabbah, D. M. Riffe, *Phys. Rev. B* **2002**, *66*, 165217; b) S. S. Prabhu, A. S. Vengurlekar, *J. Appl. Phys.* **2004**, *95*, 7803-7812; c) N. P. Wells, P. M. Belden, J. R. Demers, W. T. Lotshaw, *J. Appl. Phys.* **2014**, *116*, 073506; d) X. He, N. Punpongjareorn, C. Y. Wu, I. A. Davydov, D.-S. Yang, *J. Phys. Chem. C* **2016**, *120*, 9350-9356.

[16] a) C. Thomsen, H. T. Grahn, H. J. Maris, J. Tauc, *Phys. Rev. B* **1986**, *34*, 4129-4138; b) K. Ishioka, A. Rustagi, U. Hofer, H. Petek, C. J. Stanton, *Phys. Rev. B* **2017**, *95*, 035205.

[17] A. V. Zamkov, A. I. Zaitsev, S. A. Parshikov, A. M. Sysoev, *Inorg. Mater.* **2001**, *37*, 82-83.

[18] I. Girnyk, O. Krupych, I. Martunyuk-Lototska, F. Motsnyi, R. Vlokh, *Ukr. J. Phys. Opt.* **2003**, *4*, 165-169.

[19] a) A. J. Lehner, D. H. Fabini, H. A. Evans, C. A. Hébert, S. R. Smock, J. Hu, H. B. Wang, J. W. Zwanziger, M. L. Chabinyc, R. Seshadri, *Chem. Mater.* **2015**, *27*, 7137-7148; b) N. K. Tailor, P. Maity, S. Satapathi, *J. Phys. Chem. Lett.* **2022**, *13*, 5260-5266.

[20] S. V. Mel'nikova, A. I. Zaĭtsev, *Phys. Solid State* **1997**, *39*, 1652-1654.

[21] M. Saba, M. Cadelano, D. Marongiu, F. P. Chen, V. Sarritzu, N. Sestu, C. Figus, M. Aresti, R. Piras, A. G. Lehmann, C. Cannas, A. Musinu, F. Quochi, A. Mura, G. Bongiovanni, *Nat. Commun.* **2014**, *5*, 5049.
[22] A. V. Arakcheeva, M. Bonin, G. Chapuis, A. I. Zaitsev, *Z. Kristallogr.* **1999**, *214*, 279-283.
[23] M. Bonn, K. Miyata, E. Hendry, X.-Y. Zhu, *ACS Energy Lett.* **2017**, *2*, 2555-2562.
[24] A. Ichimiya, P. I. Cohen, *Reflection high-energy electron diffraction*, Cambridge Univ. Press, Cambridge, UK, **2004**.
[25] a) X. Wu, L. Z. Tan, X. Shen, T. Hu, K. Miyata, M. T. Trinh, R. Li, R. Coffee, S. Liu, D. A. Egger, I. Makasyuk, Q. Zheng, A. Fry, J. S. Robinson, M. D. Smith, B. Guzelturk, H. I. Karunadasa, X. Wang, X. Zhu, L. Kronik, A. M. Rappe, A. M. Lindenberg, *Sci. Adv.* **2017**, *3*, e1602388; b) B. Guzelturk, A. Lindenberg, *MRS Bull.* **2021**, *46*, 704-710; c) H. Zhang, W. Li, J. Essman, C. Quarti, I. Metcalf, W.-Y. Chiang, S. Sidhik, J. Hou, A. Fehr, A. Attar, M.-F. Lin, A. Britz, X. Shen, S. Link, X. Wang, U. Bergmann, M. G. Kanatzidis, C. Katan, J. Even, J.-C. Blancon, A. D. Mohite, *Preprint* **2022**, arXiv:2204.01145.
[26] a) G. Sciaini, R. J. D. Miller, *Rep. Prog. Phys.* **2011**, *74*, 096101; b) X. He, M. Chebl, D.-S. Yang, *Nano Lett.* **2020**, *20*, 2026-2033; c) A. Zong, A. Kogar, N. Gedik, *MRS Bull.* **2021**, *46*, 720-730; d) M. Chebl, X. He, D.-S. Yang, *Nano Lett.* **2022**, *22*, 5230-5235.
[27] X. He, D.-S. Yang, *Nano Lett.* **2021**, *21*, 1440-1445.
[28] O. V. Vakulenko, V. O. Gubanov, S. V. Kun, F. V. Motsnyi, E. Y. Peresh, V. A. Terekhov, *SPIE Proceedings* **1998**, *3359*, 351-354.
[29] A. V. Arakcheeva, G. Chapuis, M. Meyer, *Z. Kristallogr.* **2001**, *216*, 199-205.
[30] S. Y. Wei, S. J. Tie, K. Shen, H. Sun, X. J. Zheng, H. Wang, W. Q. Liang, J. H. Zou, Y. X. Huang, L. Z. Luo, X. Y. Zhou, T. X. Zeng, A. B. Ren, D. W. Zhao, J. Wu, *Adv. Opt. Mater.* **2022**, 2201585.
[31] a) A. P. Schlaus, M. S. Spencer, X.-Y. Zhu, *Acc. Chem. Res.* **2019**, *52*, 2950-2959; b) S. W. Eaton, M. L. Lai, N. A. Gibson, A. B. Wong, L. T. Dou, J. Ma, L.-W. Wang, S. R. Leone, P. D. Yang, *Proc. Natl. Acad. Sci. USA* **2016**, *113*, 1993-1998.
[32] X. Sun, Z. Gao, Y. Liu, Z. Wang, X. Wang, W. Zhang, B. Xu, X. Meng, *ACS Photonics* **2019**, *6*, 3290-3297.
[33] K. Biswas, *Mater. Adv.* **2022**, *3*, 6791-6798.
[34] M. Y. Leng, Z. W. Chen, Y. Yang, Z. Li, K. Zeng, K. H. Li, G. D. Niu, Y. S. He, Q. C. Zhou, J. Tang, *Angew. Chem. Int. Ed.* **2016**, *55*, 15012-15016.
[35] K. M. McCall, Z. Liu, G. Trimarchi, C. C. Stoumpos, W. Lin, Y. He, I. Hadar, M. G. Kanatzidis, B. W. Wessels, *ACS Photonics* **2018**, *5*, 3748-3762.
[36] X. He, N. Punpongjareorn, W. Z. Liang, Y. Lin, C. L. Chen, A. J. Jacobson, D.-S. Yang, *Sci. Rep.* **2017**, *7*, 10045.
[37] G. Kresse, D. Joubert, *Phys. Rev. B* **1999**, *59*, 1758-1775.
[38] G. Kresse, J. Furthmüller, *Phys. Rev. B* **1996**, *54*, 11169-11186.
[39] P. E. Blöchl, *Phys. Rev. B* **1994**, *50*, 17953-17979.
[40] J. P. Perdew, K. Burke, M. Ernzerhof, *Phys. Rev. Lett.* **1996**, *77*, 3865-3868.
[41] a) K. Parlinski, Z. Q. Li, Y. Kawazoe, *Phys. Rev. Lett.* **1997**, *78*, 4063-4066; b) A. Togo, F. Oba, I. Tanaka, *Phys. Rev. B* **2008**, *78*, 134106.